Vortex flow generator utilizing synthetic jets by diaphragm vibration

Van Thanh Dau[1*†], Thien Xuan Dinh[2*], Tung Thanh Bui[3] and Canh-Dung Tran[4†]

[1]*Research Group (Environmental Health), Sumitomo Chemical. Ltd, Hyogo 665-8555, Japan (dauv@sc.sumitomo-chem.co.jp; dauthanhvan@gmail.com)*
[2]*Graduate School of Science and Engineering, Ritsumeikan University, Shiga 525-8577, Japan*
[3]*University of Engineering and Technology, Vietnam National University, Hanoi, Vietnam*
[4]*School of Mechanical and Electrical Engineering, University of Southern Queensland, Australia (Canh-Dung.Tran@usq.edu.au)*
[*]Equally contributing authors
[†]Corresponding authors

Abstract: This paper develops a millimeter scale fully packaged device in which a vortex flow of high velocity is generated inside a chamber. Under the actuation by a lead zirconate titanate (PZT) diaphragm, a flow circulates with increasing velocity after each actuating circle to form a vortex in a cavity named as the vortex chamber. At each cycle, the vibration of the PZT diaphragm creates a small net air flow through a rectifying nozzle, generates a synthetic jet which propagates by a gradual circulation toward the vortex chamber and then backward the feedback chamber. The design of such device is firstly conducted by a numerical analysis whose results are considered as the base of our experimental set-up. A vortex flow generated in a chamber of the device (named as the votex chamber) was observed by a high-speed camera. The present approach which was illustrated by both the simulation and experiment is potential in various applications related to the inertial sensing, fluidic amplifier and micro/nano particle trapping and mixing.

Keywords: vortex flow, synthetic jet, confined space, PZT diaphragm, OpenFOAM

1. INTRODUCTION

Vortex flow is a potential technique to enhance the mixing and an efficient way for inertial sensing [1]–[4]. Several promising techniques to create vortex flow have been reported and can be outlined as follows. Leo et al. utilized ion wind generated between a needle and a transparent electrode to create micro vortices [5], [6]. Dunn-Rankin et al. [7] created swirl flow in an earthed cylinder by circularly arraying four pin discharge electrodes around its center. Hayakawa and his co-workers generated whirling flow by using PZT diaphragm to vibrate an array of micropillars for cell manipulation [8]. And a recent study by Zhao et al. [9] suggested the use of dual pins parallel to a grounded plate to generate vortices.

Apparently, the above configurations are designed for open systems. As we know, flow in a closed system possesses several advantages, such as independence from the contamination by environmental variations [10]–[14]. With the introduction of flow circulating in a confined space, the integration and miniaturization of measuring systems enhance the capability and impact of microfluidic systems [15]–[17]. The flow in a confined space has been applied in the inertial sensing and particularly the angular rate sensing where the presence of a self-contained valveless micro-pump reduces the risk of damage to mechanical counterparts [18]–[27].

In this context, vortex based inertial fluidic systems have been described in several publications, for example, vortex based inertial fluidic system and fluidic amplifier by NASA [28], [29], or vortex based inertial sensor found in several intellectual properties [30]–[32]. However, there has not been any sufficient technical information disclosed. More recently, Chang's group studies on multi-axis inertial sensor using the movement of the vortex in a device, nevertheless the mechanism of vortex generation was not presented [33]–[35].

From our understanding, except the use of an external pump (external source) to create vortex flows, which is bulky and expensive, the other techniques have not been adequately presented and discussed [36]. Thus, a self-package device which is capable of generating vortex flows is reported for the first time in this paper. The flow is synthesized by an actuator that consists of a cavity sealed at one end and emitting nozzles at the other end. This technique is usually mentioned as synthetic jet where the flow is rectified by means of train of vortices behind the edges of the nozzle [37] [38]. A unique advantage of the synthetic jet compared with the conventional vortex approaches is that it can be entirely

generated and developed by the air flow inside a system. Hence, jets can transfer linear momentum to the flow without any mass injection from outside over a broad range of length and timescale [39]. For the present approach, a conventional PZT diaphragm is used to actuate a circulating flow inside a closed system. At each cycle, the vibration of the PZT diaphragm creates a small net air flow through a rectifying nozzle, generates a synthetic jet which propagates by a gradual circulation toward the vortex chamber and then backward the feedback chamber. A vortex flow generated in the system by the circulating flow whose velocity can be controlled by the vibration magnitude of the PZT is investigated by both the simulation and experiment. In the framework of this research, a model to evaluate the generated vortex in a confined system is also proposed.

2. METHODOLOGY

2.1 Mechanism and design of device

The present device includes a disc-cylinder (1) with a pump chamber (6) in one side and the vortex chamber (3) on the other side as described in Fig. 1. The pump chamber (6) is connected with the vortex chamber (3) by four driving channels (2) with a diameter of 1.5 mm each at the outer most of the cylinders and through a rectifying nozzles (5). At the center of disc-cylinder, a feedback chamber (7) with a diameter of 12.0 mm links with the vortex chamber (3) via a feedback channel (4), diameter of 3.0 mm. The total size of the device is 20 mm diameter and 5.5 mm depth.

On the device mechanism, the pump chamber is actuated by a PZT diaphragm (8) (Murata Ltd.) consisting of 100-µm-thick ceramic PZT and 120-µm-thick metal layers, which periodically vibrates under an applied voltage. The PZT vibration makes the volume of pump chamber (6) shrinking and swelling, thus air/gas inside the pump chamber is expelled and sucked alternatively. By the expelling and sucking processes, gas/air moves through a rectifying nozzle (5) and a small net flow is formed in each driving channel (2) at each cycle [40]. The net flow propagates by a gradual circulation toward the feedback chamber (7) and then backward the vortex chamber (3) through the rectifying nozzles (5) as shown in Fig. 1a. In fact, the feedback flow which accumulates momentum dramatically amplifies the rectifying effect of the nozzle [41], [42]. Therefore, the velocity of air flow increases and reaches a stably maximum value inside the vortex chamber after several circulations.

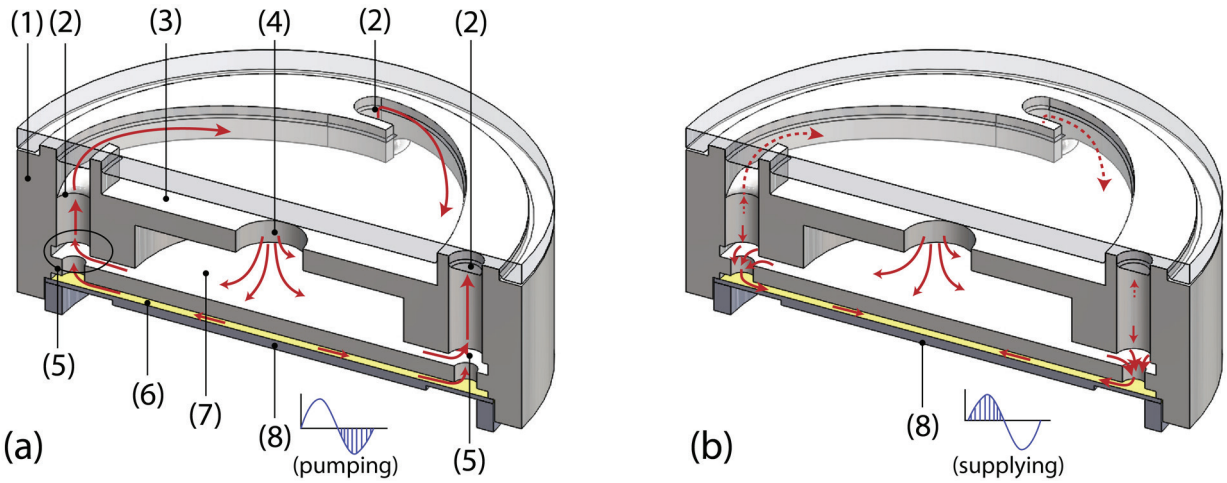

Figure 1. Mechanism of the present device: (a) flow actuated initially by the vibration of a PZT diaphragm and then rectified by nozzle; and (b) Flow moves from the driving channel to the vortex chamber and make a new circulation. (1) Disc-cylinder, (2) driving channel, (3) vortex chamber, (4) feedback channel, (5) rectifying nozzle, (6) pump chamber, (7) feedback chamber and (8) PZT diagram. Arrows show the movement of air.

After moving through driving channels, air moves into a channel across four driving channels outlets where the velocities of air flows are tangential with the chamber edges (Figs.1 and 2). If the kinetics of air flows accumulated during the circulation is strong enough, a flow vortex is generated inside the chamber and the velocity contours of air flow are surrounding the center of the feedback channel. The chamber is hence named as the vortex chamber.

In the case if the kinetics of air flows going out from driving channels is not enough, air flows are sucked into the center of vortex chamber which is considered as the sink of air flow. In other works, flow will be directly drawn into the sink.

The velocity and then kinetics of flow which yields the flow characteristic in the vortex chamber, is ultimately controlled by the vibration magnitude of the diaphragm and will be studied in the next sections.

In this work, since the outer edge of the vortex chamber is designed with a higher curvature compared with one of the outlet gate, i.e., the edge of the vortex chamber is slightly concave, flows maintain the feedback while rotating as vortexes.

2.2 Governing equations and boundary conditions

Since air is trapped and circulates inside a closed device, the flow is self-generated by vibrating pump without any inlet or outlet. The generated flow in the device is considered compressible and is governed by the following system of conservation equations:

$$\frac{\partial \rho}{\partial t} + \nabla \cdot \rho\vec{u} = 0 \tag{1}$$

$$\frac{\partial \rho\vec{u}}{\partial t} + (\vec{u} \cdot \nabla)\rho\vec{u} = -\nabla p + \nabla \cdot (\mu \nabla \vec{u}) \tag{2}$$

$$\frac{\partial \rho c_p T}{\partial t} + (\vec{u} \cdot \nabla)\rho c_p T = \nabla \cdot (\lambda \nabla T) \tag{3}$$

where $\vec{u}$, p, and T are the velocity vector, pressure, and temperature of the flow, respectively; $\mu = 1.789 \times 10^{-5}$ Pas, $\rho = 1.2041$ kgm^{-3}, $\lambda = 2.42 \times 10^{-3}$ Wm^{-1}K^{-1}, and $c_p = 1006.43$ Jkg^{-1}K^{-1} the dynamic viscosity, density, thermal conductivity, and specific heat of air, respectively. The pressure and density satisfy the state equation of ideal gas as $p = \rho R_u T/M_w$, where $R_u = 8.314$ Jmol^{-1}K^{-1} is the universal air constant and $M_w = 28.96$ gmol^{-1} the molecular weight.

The boundary condition set up on a diaphragm is derived by its vibrating rate: $v(\vec{r}, t) = 2\pi f Z \cos(2\pi f t)\, \varphi(\vec{r})$, where $\varphi(r)$ is the shape function as $\varphi(r) = (1 - (r/a)^2)^2$, with a the diaphragm radius, Z the center deflection of the PZT diaphragm and f = 4.7 kHz the vibrating frequency taken from experiment (section 4)

A 3-dimension model of the designed device together with its meshing for the simulation are presented in Fig. 2. The transient solution of Eqs. (1) - (3) is achieved using our program code developed in OpenFOAM [43] and results are discussed in section 3.

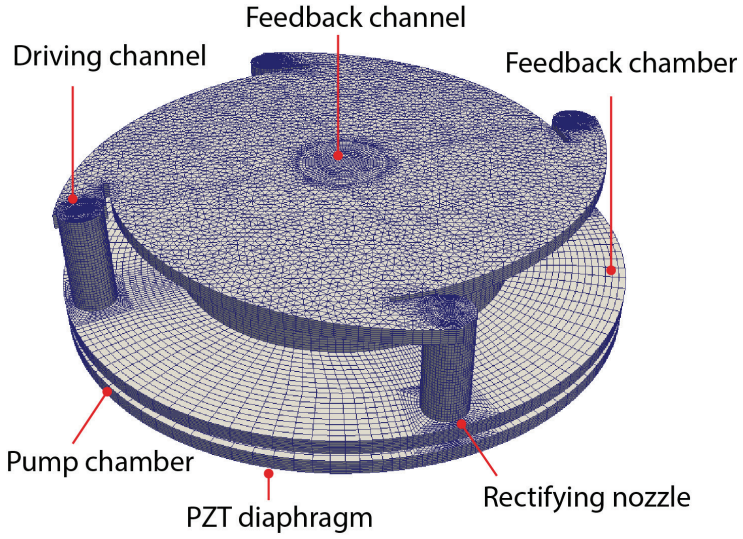

Figure 2. Decomposing the present device into structured mesh.

2.3 Experimental setup

A transparent prototype made of polypropylene of the designed system described in section 2.2 is given in Fig. 3. Two versions of the device are carried out to investigate the appearance of vortex flow using a high-speed camera and/or hotwire anemometry.

For visual evaluation, particles are introduced in the device. In order to observe the vortex appearance in the chamber, a transparent cover of the chamber is used and a high-speed camera, triggered by the power source of PZT membrane, is set up to capture the motion of particles (see Fig. 3). The PZT diaphragm is activated by sinusoidal signals from a function generator 33522A (Agilent Ltd.,) and an amplifier HAS 4051 (NF Ltd.).

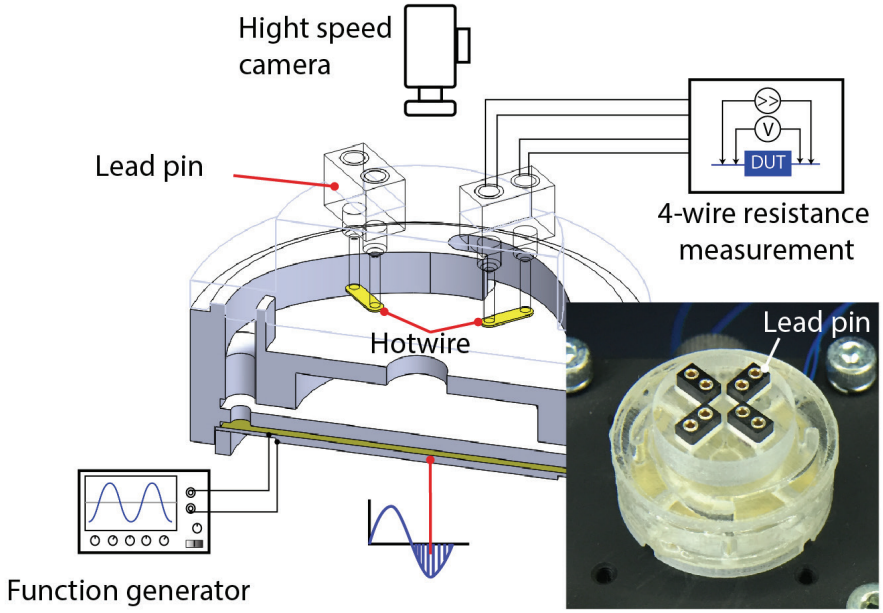

Figure 3. A schema of the designed device. Inset is a photo of the real device. The PZT diaphragm is installed underneath and the lead pin on the top of the device.

For the quantitative evaluation, a system of four tungsten hotwires (W-461057, Nillaco Ltd) with the length of 2.0 mm and diameter of 20 µm each is set up inside the vortex chamber to characterize the particle flow. Lead pins (Preci-Dip) installed on the cover of vortex chamber work as hotwire holders. A constant current is supplied to hotwires whose voltage is monitored by a TEXIO DC power supplier (PW18-1.8AQ). The ambient environment is maintained at the standard room conditions (22–25C, 60% RH). A schema of the experimental setup is represented in Fig. 3.

The average velocities of flow at four hotwire positions are measured and then compared with those by the numerical simulation.

3. NUMERICAL RESULTS AND DISCUSSIONS

Figure 4 represents the velocity field of air flow in the middle plane of vortex chamber with different deflections of a PZT diaphragm. The velocity contour of the flow by Fig. 4b depicts a vortex generated inside the chamber (red arrows) with a PZT diaphragm deflection Z of 20 µm. Meanwhile, if the PZT diaphragm deflection is not sufficient (Fig. 4a with deflection of 10 µm), flow is sucked back to the feedback chamber (described by red arrows) and thus, no vortex is created.

The above observations need to be quantitatively illustrated. Firstly, the averaging velocity was taken after the flow in the device reached the quasi steady state and was recorded for 20 cycles. Since the flow is driven by four periodic inlets from the driving channels (see Fig. 2) and then moves into the tube at the center (Fig. 4a), the flow is similar to a tornado-like vortex pattern. However, as the flow eventually moves out of the vortex chamber to re-circulate through a rectifying nozzle, it includes two components: vortex and sink. In order to analyze the flow characteristics, the flow is considered as a superposition of a blob vortex and a sink potential flow.

In fact, while the vortex is requested being created in the chamber, the sink appears inevitably in a circulatory system. Such a flow is generated and then circulates through a rectifying nozzle to complete a cycle of the flow.

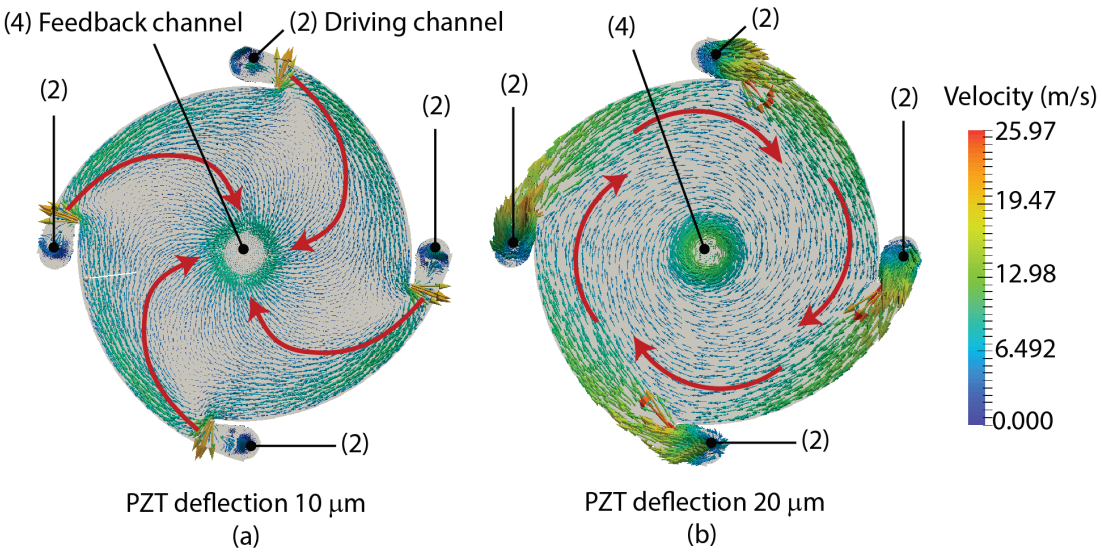

Figure 4. Numerical simulation: Observing vortex by velocity contours from top view in the vortex chamber. (a) Unobservable vortex with PZT deflection of 10 μm; and (b) Clear vortex (red arrows) caused by PZT deflection of 20 μm.

Let U_r, U_θ be the components of the averaged velocity in a circulating cycle on the radial and azimuth directions. They are given by

$$U_r(r) = \frac{1}{2\pi}\int_0^{2\pi} u_r(r,\theta)d\theta\,, \tag{4}$$

$$U_\theta(r) = \frac{1}{2\pi}\int_0^{2\pi} u_\theta(r,\theta)d\theta, \tag{5}$$

where $u_r(r, \theta)$ and $u_\theta(r, \theta)$ are the radial and azimuth components of the local time-averaged velocity, respectively. While the radial component contributes to the sink flow, the azimuth component creates the vortex.

Since the flow is described by a vortex and a sink, the velocity profile of flow would be expressed by Lamb-Oseen vortex model [44] where its components $U_\theta(r)_{vortex}$ and $U_r(r)_{sink}$ are for the vortex and for the sink, respectively

$$U_r(r)_{sink} = \frac{K_r}{2\pi r}\left(1 - e^{-r^2/{\epsilon_r}^2}\right), \tag{6}$$

$$U_\theta(r)_{vortex} = \frac{K_\theta}{2\pi r}\left(1 - e^{-r^2/{\epsilon_\theta}^2}\right), \tag{7}$$

where K_θ and K_r are constants and depict the strength of vortex and sink; respectively; and ϵ_θ and ϵ_r the core radii of the blob vortex and the sink (sink width), respectively.

The simulated U_r and U_θ with respect to the radial distance (r) are presented in Figs. 5a & b. The fitting curves of U_r, U_θ by Eqs. (4) & (6) and Eqs. (5) & (7), are respectively approximated by the least square method (LSM) for two different cases of PZT deflections.

With the vibration amplitude of 20 um, the fitting by Eqs. (4) - (7) using LSM as shown in Fig. 5b yields K_r= 59.4×10^{-3} m^2/s, K_θ = 82.7×10^{-3} m^2/s, ϵ_r = 1.63 mm, and ϵ_θ = 0.75 mm. Results by Fig. 5b show that the simulated U_θ matches the fitting curve until r reaches 3 mm before they start diverging from each other. Meanwhile the simulated U_r fits well with its fitting curve in an area with r > 3 mm. In other words, the flow is considered as a vortex with a strength of K_θ= 82.7×10^{-3} m^2/s on an area of 3 mm radius from the center; but as a sink flow with the strength of K_r = 59.4×10^{-3} m^2/s outside the vortex with r > 3 mm.

Similarly, Fig. 5a presents the radial and azimuth velocities (U_r, U_θ) plotted versus the radial distance by the numerical simulation with a smaller PZT vibration of 10μm. The approximated values of K_r and K_θ by the fitting method are 39.2×10^{-3} m^2/s, 15.7×10^{-3} m^2/s, respectively. Results depict that with a decrease of the PZT deflection, the size and strength of vortex reduce (r = 2 mm and K_θ= 15.7×10^{-3} m^2/s by Fig. 5a compared with r = 3 mm and K_θ= 82.7×10^{-3} m^2/s in Fig. 5b). Furthermore, the sink strength (K_r = 39.2×10^{-3} m^2/s) is much stronger than the vortex one (K_θ= 15.7×10^{-3}

m^2/s). This indicates that the flow in this case with a small PZT vibration is mostly a sink (i.e., the flow is directly drifted from the inlet to the outlet) and the formed vortex is not significant.

The impact of PZT vibration amplitude on the vortex and sink components in the chamber is presented in Fig. 6. Numerical results by Fig. 6 demonstrate that while an increase of the vibration amplitude yields strongly increasing the flow momentum and then the vortex strength (K_θ) (from 15.7 to 127.7×10^{-3} m^2/s) in the chamber, it does not affect significantly on the vortex width ϵ_θ (with an variation of around 8%, i.e, approximately 0.78 ± 0.08) because of the confined geometry of the vortex. Results also show that an increase of diaphragm vibration amplitude would bring the vortex closer to the center of the feedback channel with a designed radius of 1.5mm (see Fig. 2) and a swirl is expected in this channel. This characteristic is important for the development of vortex – sink angular rate sensor [36].

Hence, the flow in the present configuration consists of two components: vortex and sink. The sink is to create a circulating flow going through the feedback channel. It can be found that (*i*) the radius of vortex ϵ_θ is about 0.78 mm, slightly longer than half-radius of feedback channel; and (*ii*) the central region of the feedback inlet acts as a sink but not a vortex.

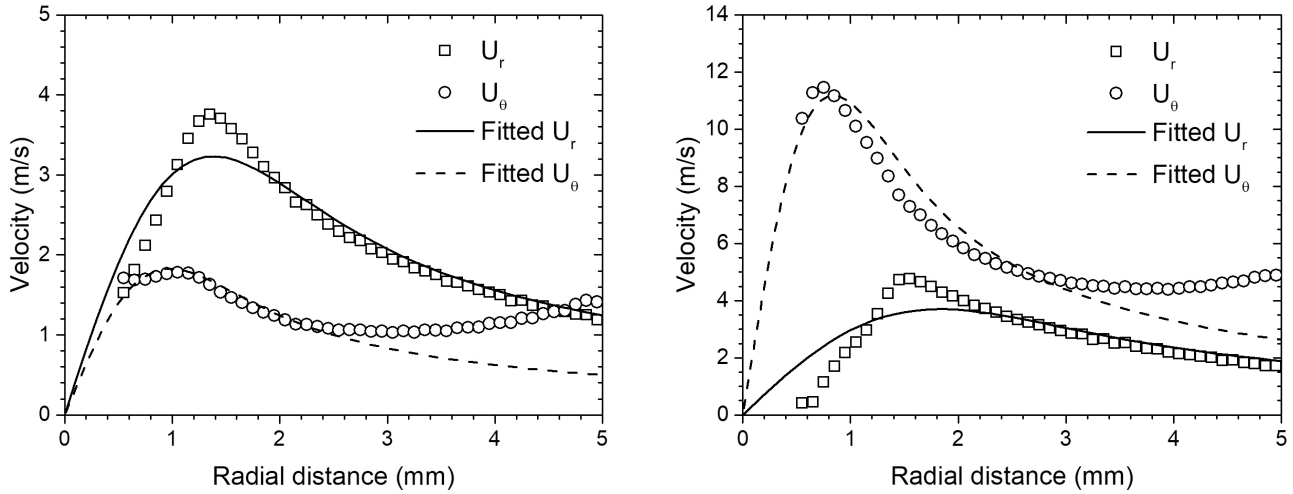

Figure 5. The radial and azimuth velocities (U_r, U_Θ) plotted versus the radial distance by the simulation and their fitting curves for two PZT deflections of 10 μm (Fig. 5a) and 20 μm (Fig. 5b). The velocity components U_r, U_Θ by the simulation are denoted by square and circle symbols, respectively and the fitting curves of U_r, U_Θ by the solid and dashed lines, respectively.

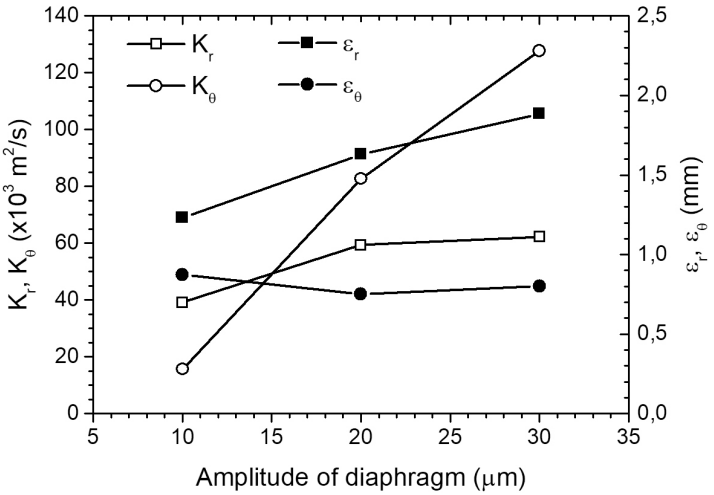

Figure 6. K_r, K_θ, ϵ_r and ϵ_θ of flow in vortex chamber plotted versus the vibration amplitude of PZT.

Furthermore, an amplitude increase of the diaphragm vibration yields the increasing of both sink strength K_r (from 39.2 3×10^{-3} m^2/s to 62.3 $\times 10^{-3}$ m^2/s, see Fig. 5) and sink width ϵ_r of 28% (from 1.23 mm to 1.88 mm, see Fig. 6). The finding can be explained as follows. The higher amplitude of PZT vibration is, the higher flowrate moves in the vortex chamber and thus, the higher flowrate (i.e., stronger K_r) moves out through the feedback channel. Besides, the increase of sink width ϵ_r can be caused by the geometry of the vortex chamber. Indeed, since the curvature of the outer edge of the chamber is higher than the outlet gate, the sink flow is always formed to smooth feedback flow, yielding a stronger and also earlier sink flow at the increase of the vibration amplitude of diaphragm. Finally, our numerical simulation also shows that a magnitude of 20 µm of the PZT vibration for the present configuration is sufficient to generate a good vortex in the chamber. On the other hand, if the PZT diaphragm vibrates with an amplitude less than 10 µm then no observable vortex appears and hence the flow primary operates as a sink in the chamber.

4. EXPERIMENTAL RESULTS, CHARACTERISATION AND DISCUSSIONS

4.1 Investigation of vortex flow using high-speed camera

The snapshots of particles' tracks observed 500 ms after a start-up time T_0 (T_0, T_0 + 500 ms; $T_0 \approx$ 5s in this work) by a high-speed camera are presented in Fig. 7 for a range of voltage (20, 30, 40 and 50 V) applied on the diaphragm. The observation demonstrates that vortex flow only appears in the chamber of the device until the driving voltage applied on the PZT diaphragm overcame 20 V. A vortex is initially formed when V_{PZT} reaches 30 V and becomes clear at V_{PZT} of 50 V. The experimental clips also depict, no observable vortex but a tracking of particles moves directly from the inlet (driving channel) to the outlet (feedback channel) inside the vortex chamber when V_{PZT} = 20 V. It is worth noting that this observation is in good agreement with simulated results in section 3. The higher voltage is applied on the diaphragm, the stronger and clearer vortex appears in the chamber. Moreover, the vortex flow generated in the vortex chamber is almost symmetric. Readers are politely encouraged to refer visual illustrations with a high resolution in attached supplementary files which represent much clearer flows of particles from four driving channels.

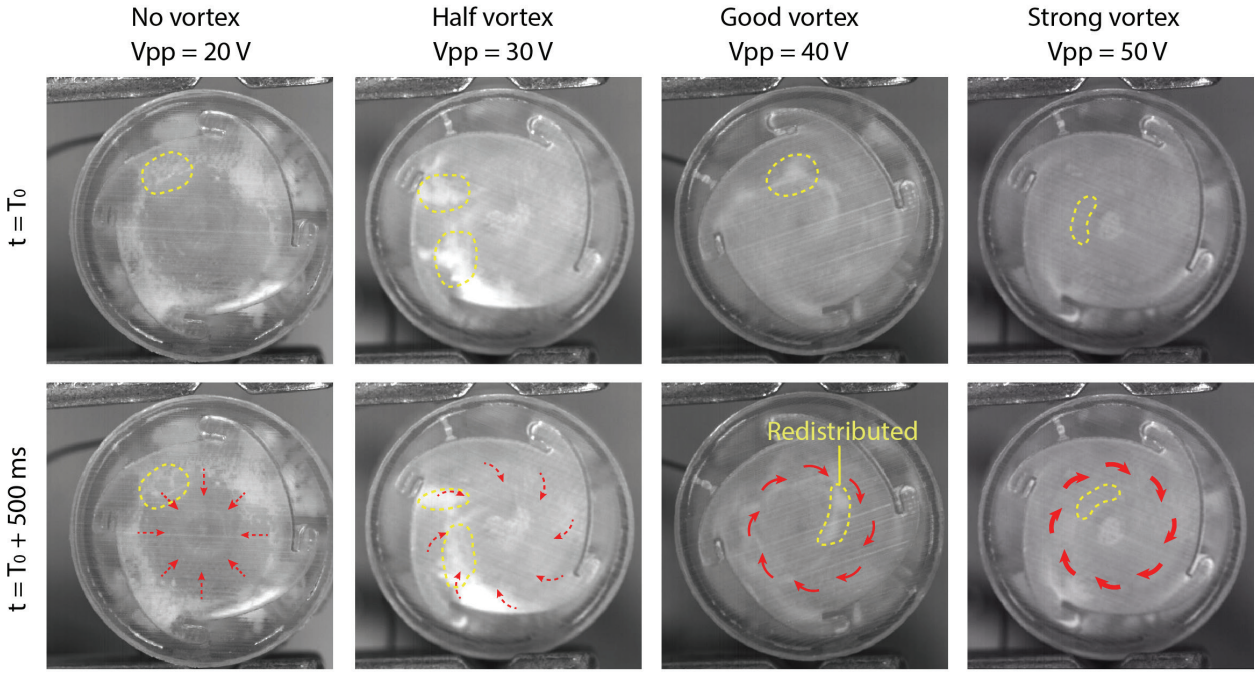

Figure 7. Images of flow inside the vortex chamber at several times (T_0, T_0 + 500ms) with a range of voltages applied on the PZT diaphragm (20, 30, 40 and 50V), T_0 is the start-up time ($T_0 \approx$ 5 seconds in this work). Readers are politely encouraged to watch corresponding video clips in supplementary files for clearer visualizations. "No vortex" indicates the vortex is not observable during the current experimental setup.

4.2 Characterization of vortex flow using hotwire anemometry

In order to characterize the vortex flow, the velocity of flow at several positions in the vortex chamber is measured using four hotwires which are installed as shown in Fig. 3. Hotwires are heated by a constant current (I) of 200 mA.

When the PZT diaphragm vibrates, an air flow is generated and hotwires are hence cooled by the forced convection. The relative voltage on hotwires can be directly determined by $V_{HW} = I\Delta R_{HW} = I\alpha\Delta T$, with α the temperature coefficient of resistance of the hotwire, ΔR_{HW} and ΔT the variations of resistance and hotwires, respectively.

The relationship between the voltage on hotwires and the applied voltage frequency is presented in Fig. 8a with a given voltage of V_{PZT} = 50 V applied on the diaphragm and a hotwire heating current of 200 mA. Results show that the voltage on hotwires increases and reaches a peak value of 4.20 mV at the frequency of 4.67 kHz and then decreases with the increase of the frequency.

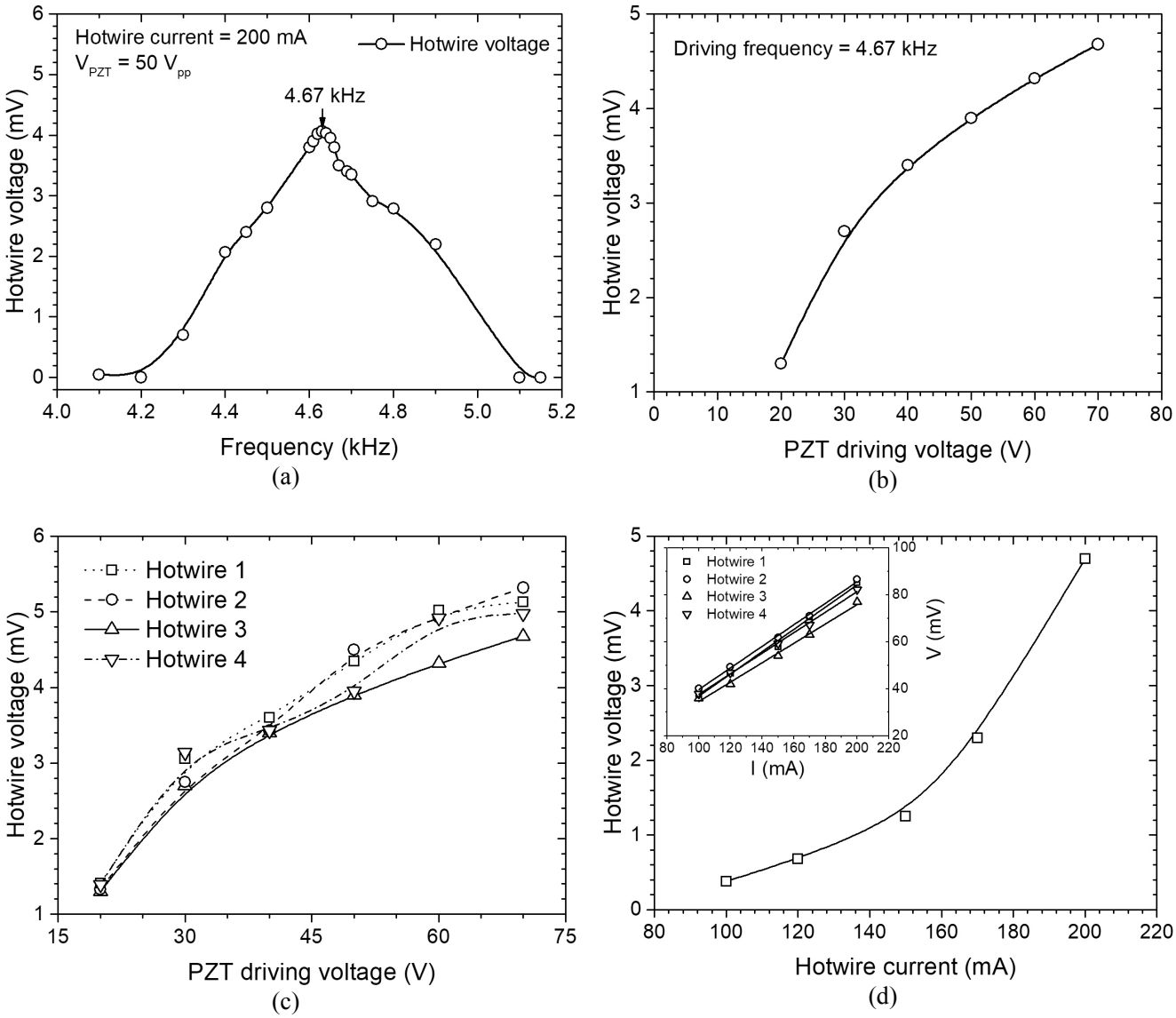

Figure 8. Hotwire voltage plotted versus (a) the vibration frequency on the PZT with the resonant frequency of 4.67 kHz; (b) the voltage applied on the PZT using a driving frequency of 4.67 kHz; (c) the voltage applied on the PZT for four hotwires with a driving frequency of 4.67 kHz and a heating current of 200 mA and (d) the hotwire heating current using a voltage of 70 V with driving frequency of 4.67 kHz applied on the PZT diaphragm (the inset shows the I-V characteristic of 4 hotwires without pump (V_{PZT} = 0)).

Moreover, experimental results in Fig. 8b depict a general increase of V_{HW} with the increase of voltage applied on the PZT diaphragm. Indeed, the higher voltage applied on PZT diaphragm yields the larger deflection and then the stronger

flow. Furthermore, the experiment also shows that hotwires cannot capture signal from the flow with voltages less than 20 V (see Fig. 8b) and thus, a minimum voltage of 20 V is necessary to circulate the flow throughout the device at a considerable flow rate. In addition, the voltages measured on the four hotwires with respect to PZT driving voltage using a pump vibration of 4.67 kHz and heating current of 200 mA are almost the same as presented in Fig. 8c. This indicates that flows through four hotwires are relatively similar.

Finally, the experiment also depicts that the voltages measured on hotwires sharply increase with the increasing of heating current as shown in Fig. 8d. As the current-voltage characteristic of hotwires described in the inset of Fig. 8d expresses a constant resistance (0.446 +/- 0.026 Ω) of four hotwires during the heating process, this strong increase of the hotwire voltage with respect to the heating current can be explained by Ohm's law and the heat transfer. For the present system, the heating current is considered as a governing parameter to adjust the working condition of the device [39].

The voltage of hotwires is used to determine the average velocity of flow at local areas around hotwire positions by comparing the heat transfer coefficient of forced convection$(0.24 + 0.56Re^{0.45}\,\lambda/D)$ with one by the natural convection $(1.02Ra^{0.1}\,\lambda/D)$ of air with λ, Ra and d the thermal conductivity, Rayleigh number, effective diameter of the hotwire, respectively; and Re the Reynolds number of air flow. The calculation is carried out using our subroutine C-code whose details can be found in our recent publications [45], [46].

By the procedure mentioned above, the average velocity of flow calculated from hotwire voltages in Fig. 8b yields the relationship of the velocity of flow with respect to the PZT driving voltage as presented in Fig. 9. Experimental results by Fig. 9 show a linear increase of flow velocity with the increase of PZT driving voltage (presented by the line of square symbols).

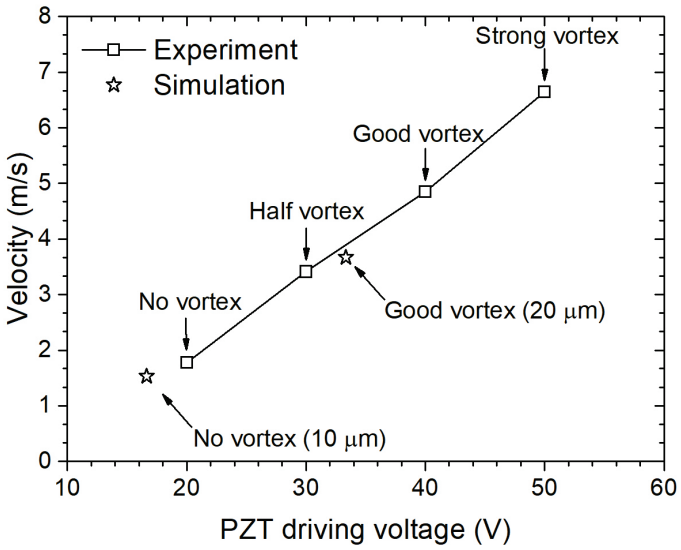

Figure 9. Average velocity of flow at hotwire areas in the vortex chamber converted from hotwire voltage recorded by experimental work which is presented in Fig. 8b. "No vortex" indicates the vortex is not observable during the current experimental setup.

Similarly, in coupling with the relation of the amplitude of PZT to the voltage applied on the PZT diaphragm which was established by our recent work [12][15], the simulated velocity of flow is also plotted versus the PZT driving voltage in Fig. 9 (line of star symbols).

It can be seen that although the relationship between the flow velocity measured at hotwire positions and the PZT driving voltage by the experiment is in good agreement with one by the simulation as presented in Fig. 9, the vortex appearances by experimental observation are slightly slower than those in the numerical simulation. Indeed, results depict that the PZT driving voltage measured by the experiment seems to be higher than one by the simulation for the vortex evolution. For example, meanwhile the experiment found that a vortex will not appear until the PZT driving voltage is stronger than 20 V and it becomes fully clear at a PZT driving voltage of around 40 V, the corresponding values of PZT driving voltage by the simulation are 17 V and 34 V, respectively.

This difference can be explained as follows. Vortex appeared in the chamber is followed up by the track of particles suspended in air. Since the velocity of particles is slower than the air velocity, the vortex is found at a higher velocity of air and then at a higher driving voltage applied on the PZT diagram as shown in Fig. 9.

It is worth noting that the relationship of the average velocity of flow to the PZT driving voltage by Fig. 9 yields the determination of a relevant PZT driving voltage for a vortex appearance in the device. For example, a PZT driving voltage of 40 V would create a good vortex (see Fig. 7) with velocity of around 5 m/s as shown in Fig. 9.

5. CONCLUSIONS

A millimeter scale fully packaged device which generates a vortex flow of high velocity is reported. The synthetic jet flow actuated by a PZT diaphragm whose velocity increases after each circulation forms a vortex in a desired chamber. The design of the device is firstly conducted by a numerical analysis whose results are referred as the base of our experiment. Experimental results are in good agreement with our numerical prediction and a flow vortex is observed by a high-speed camera. Both the numerical and experimental results demonstrate the potential of the device in various applications related to inertial sensing, fluidic amplifier and micro/nano particle trapping and mixing.

REFERENCE

[1] P. Meunier and E. Villermaux, "How vortices mix," *J. Fluid Mech.*, vol. 476, no. 476, pp. 213–222, 2003.

[2] S. J. Liu, H. H. Wei, S. H. Hwang, and H. C. Chang, "Dynamic particle trapping, release, and sorting by microvortices on a substrate," *Phys. Rev. E - Stat. Nonlinear, Soft Matter Phys.*, vol. 82, no. 2, 2010.

[3] P. K. Wong, T.-H. Wang, J. H. Deval, and C.-M. Ho, "Electrokinetics in Micro Devices for Biotechnology Applications," *IEEE/ASME Trans. Mechatronics*, vol. 9, no. 2, pp. 366–376, Jun. 2004.

[4] Rexford Donald L, "Vortex fluid amplifier circuit for controlling flow of electrically conductive fluid," US3654943, 1970.

[5] L. Y. Yeo and J. R. Friend, "Electrohydrodynamic Flow for Microfluidic Mixing and Microparticle Manipulation," in *International Symposium on Electrohydrodynamics (ISEHD), Buenos Aires Argentina*, 2014, no. December, pp. 4–7.

[6] L. Y. L. Yeo, D. Hou, S. Maheshswari, and H.-C. C. Chang, "Electrohydrodynamic surface microvortices for mixing and particle trapping," *Appl. Phys. Lett.*, vol. 88, no. 23, pp. 2006–2008, 2006.

[7] F. Weinberg, F. Carleton, D. Kara, A. Xavier, D. Dunn-Rankin, and M. Rickard, "Inducing gas flow and swirl in tubes using ionic wind from corona discharges," *Exp. Fluids*, vol. 40, no. 2, pp. 231–237, 2006.

[8] T. Hayakawa, S. Sakuma, and F. Arai, "On-chip 3D rotation of oocyte based on a vibration-induced local whirling flow," *Microsystems Nanoeng.*, vol. 1, no. March, p. 15001, 2015.

[9] P. Zhao, S. Portugal, and S. Roy, "Efficient needle plasma actuators for flow control and surface cooling," *Appl. Phys. Lett.*, vol. 107, no. 3, p. 33501, 2015.

[10] K. D. Dorfman, M. Chabert, J.-H. Codarbox, G. Rousseau, P. de Cremoux, and J.-L. Viovy, "Contamination-free continuous flow microfluidic polymerase chain reaction for quantitative and clinical applications.," *Anal. Chem.*, vol. 77, no. 11, pp. 3700–4, Jun. 2005.

[11] V. T. Dau, T. X. Dinh, and T. T. Bui, "Jet flow generation in a circulatory miniaturized system," *Sensors Actuators B Chem.*, vol. 223, pp. 820–826, 2015.

[12] Tung Thanh Bui, Thien Xuan Dinh, Phan Thanh Hoa, and Van Thanh Dau, "Study on the PZT diaphragm actuated multiple jet flow in a circulatory miniaturized system," in *2015 IEEE SENSORS*, 2015, pp. 1–4.

[13] T. X. Dinh, D. B. Lam, C.-D. Tran, T. T. Bui, P. H. Pham, and V. T. Dau, "Jet flow in a circulatory miniaturized system using ion wind," *Mechatronics*, vol. 47, no. September, pp. 126–133, Nov. 2017.

[14] L. B. Dang, T. X. Dinh, T. T. Bui, T. C. Duc, H. T. Phan, and V. T. Dau, "Ionic JET flow in a circulatory miniaturized system," in *2017 19th International Conference on Solid-State Sensors, Actuators and Microsystems (TRANSDUCERS)*, 2017, pp. 2099–2102.

[15] V. T. Dau and T. X. Dinh, "Numerical study and experimental validation of a valveless piezoelectric air blower for fluidic applications," *Sensors Actuators B Chem.*, vol. 221, pp. 1077–1083, Jul. 2015.

[16] L. Y. Yeo, H. C. Chang, P. P. Y. Chan, and J. R. Friend, "Microfluidic devices for bioapplications," *Small*, vol. 7, no. 1, pp. 12–48, 2011.

[17] Y. H. Seo, H. J. Kim, W. K. Jang, and B. H. Kim, "Development of active breathing micro PEM fuel cell," *Int. J. Precis. Eng. Manuf. Technol.*, vol. 1, no. 2, pp. 101–106, 2014.

[18] V. T. Dau, D. V. Dao, T. Shiozawa, H. Kumagai, and S. Sugiyama, "A Single-Axis Thermal Convective Gas Gyroscope," *Sensors Mater.*, vol. 17, no. 8, pp. 453–463, 2005.

[19] V. T. Dau, D. V. Dao, T. Shiozawa, H. Kumagai, and S. Sugiyama, "Development of a dual-axis thermal convective gas gyroscope," *J. Micromechanics Microengineering*, vol. 16, no. 7, pp. 1301–1306, Jul. 2006.

[20] V. T. Dau, T. X. Dinh, D. V. Dao, and S. Sugiyama, "Design and Simulation of a Novel 3-DOF MEMS Convective Gyroscope," *IEEJ Trans. Sensors Micromachines*, vol. 128, no. 5, pp. 219–224, May 2008.

[21] S. Liu and R. Zhu, "Micromachined Fluid Inertial Sensors," *Sensors*, vol. 17, no. 2, p. 367, Feb. 2017.
[22] H. Cao, H. Li, J. Liu, Y. Shi, J. Tang, and C. Shen, "An improved interface and noise analysis of a turning fork microgyroscope structure," *Mech. Syst. Signal Process.*, vol. 70–71, pp. 1209–1220, Mar. 2016.
[23] H. Cao *et al.*, "Sensing mode coupling analysis for dual-mass MEMS gyroscope and bandwidth expansion within wide-temperature range," *Mech. Syst. Signal Process.*, vol. 98, pp. 448–464, Jan. 2018.
[24] V. T. Dau, T. Otake, T. X. Dinh, D. V. Dao, and S. Sugiyama, "A multi axis fluidic inertial sensor," in *Proceedings of IEEE Sensors*, 2008, vol. 1, pp. 666–669.
[25] P. T. Hoa, T. X. Dinh, and V. T. Dau, "Design Study of Multidirectional Jet Flow for a Triple-Axis Fluidic Gyroscope," *IEEE Sens. J.*, vol. 15, no. 7, pp. 4103–4113, Jul. 2015.
[26] Dzung Viet Dao, S. Okada, Van Thanh Dau, T. Toriyama, and S. Sugiyama, "Development of a 3-DOF silicon piezoresistive micro accelerometer," in *Micro-Nanomechatronics and Human Science, 2004 and The Fourth Symposium Micro-Nanomechatronics for Information-Based Society, 2004.*, 2004, pp. 1–6.
[27] R. Amarasinghe, D. V Dao, V. T. Dau, and S. Sugiyama, "Ultra miniature novel three-axis micro accelerometer," in *Proceedings of IEEE Sensors*, 2009.
[28] Weathers and T. M., "NASA contributions to fluidic systems: A survey," Jan. 1972.
[29] G. L. Goglia and D. K. Patel, "An experimental and theoretical study of the flow phenomena within a vortex sink rate sensor," 1974.
[30] R. E. Bowles, "Gyroscopic fluid control device," US3509778, 1970.
[31] R. J. Reilly, "Fluid vortex apparatus," US3340737, 1967.
[32] R. E. Bowles, "Fluid control device," US3,410,143, 1968.
[33] H. Chang, P. Zhou, X. Gong, J. Xie, and W. Yuan, "Development of a tri-axis vortex convective gyroscope with suspended silicon thermistors," in *2013 IEEE SENSORS*, 2013, pp. 1–4.
[34] H. Chang, P. Zhou, Z. Xie, X. Gong, Y. Yang, and W. Yuan, "Theoretical modeling for a six-DOF vortex inertial sensor and experimental verification," *Journal of Microelectromechanical Systems*, vol. 22, no. 5. pp. 1100–1108, 2013.
[35] H. Chang *et al.*, "On Improving the Performance of a Triaxis Vortex Convective Gyroscope Through Suspended Silicon Thermistors," *IEEE Sens. J.*, vol. 15, no. 2, pp. 946–955, 2015.
[36] T. Sarpkaya, "A pneumatic vortex angular rate sensor - analysis and experiments," *Automatica*, vol. 9, no. 1 (January, 1973), pp. 29–34, 1973.
[37] B. L. Smith and A. Glezer, "The formation and evolution of synthetic jets," *Phys. Fluids*, vol. 10, no. 9, p. 2281, Sep. 1998.
[38] L. S. . Kovasznay, H. Fujita, and R. . Lee, *Advance in Geophysics 18B*. 1975.
[39] A. Glezer and M. Amitay, "Synthetic jets," *Annu. Rev. Fluid Mech.*, vol. 34, no. 1, pp. 503–529, Jan. 2002.
[40] T. X. Dinh, V. T. Dau, S. Sugiyama, and P. H. Pham, "Fluidic device with pumping and sensing functions for precise flow control," *Sensors Actuators, B Chem.*, vol. 150, no. 2, pp. 819–824, Oct. 2010.
[41] H. Phan, T. Dinh, P. Bui, and V. Dau, "Transient Characteristics of a Fluidic Device for Circulatory Jet Flow," *Sensors*, vol. 18, no. 3, p. 849, Mar. 2018.
[42] V. T. Dau, T. X. Dinh, C. D. Tran, P. N. Bui, D. D. Vien, and H. T. Phan, "Fluidic mechanism for dual-axis gyroscope," *Mech. Syst. Signal Process.*, vol. 108, pp. 73–87, 2018.
[43] OpenFOAM®, "OpenFOAM® | The OpenFOAM Foundation," 2016. .
[44] M. J. Bhagwat and J. G. Leishman, "Generalized Viscous Vortex Model for Application to Free-Vortex Wake and Aeroacoustic Calculations," *Annu. Forum Proceedings-American Helicopter Soc.*, no. June, pp. 2042–2057, 2008.
[45] V. T. Dau, T. X. Dinh, T. T. Bui, C. D. Tran, H. T. Phan, and T. Terebessy, "Corona based air-flow using parallel discharge electrodes," *Exp. Therm. Fluid Sci.*, vol. 79, pp. 52–56, 2016.
[46] V. T. Dau, C. D. Tran, T. T. Bui, V. D. X. Nguyen, and T. X. Dinh, "Piezo-resistive and thermo-resistance effects of highly-aligned CNT based macrostructures," *RSC Adv.*, vol. 6, no. 108, pp. 106090–106095, 2016.